applied sciences

MDPI

Article

Estimation of Grain Size and Composition in Steel Using Laser UltraSonics Simulations at Different Temperatures

Arno Duijster [1,*], Arno Volker [1], Frenk Van den Berg [2] and Carola Celada-Casero [3]

[1] TNO, 2597 AK The Hague, The Netherlands
[2] Tata Steel, 1970 CA IJmuiden, The Netherlands
[3] National Centre for Metallurgical Research (CENIM-CSIC), 28040 Madrid, Spain
* Correspondence: arno.duijster@tno.nl

Abstract: The applicability of laser ultrasonics for the determination of grain size and phase composition in steels under different temperatures was investigated. This was done by obtaining the velocity and attenuation of propagating ultrasonic waves in a simulated steel medium. Samples of ferrite and austenite with varying microstructures were modelled and simulated with the finite difference method, as were samples with varying ratios of austenite and martensite. The temperature of the medium was taken into account as an essential parameter, since both velocity and attenuation are temperature dependent. Results of the velocity and attenuation analysis showed that the use of the wave propagation velocity is not feasible for determination of grain size or phase composition due to a high sensitivity to temperature and sample thickness. The frequency-dependent ultrasonic wave attenuation was less sensitive to the variation of temperature and sample thickness. It can be concluded that accurate knowledge of the temperature is essential for obtaining a correct grain size or phase ratio estimation: a temperature accuracy of 100 °C yields a grain size accuracy in the order of a micrometer using the attenuation. Similarly, a temperature accuracy of 70 °C leads to a phase ratio estimation accuracy of 10%.

Keywords: laser ultrasonics; non-destructive testing; steel; microstructure; multiphase; temperature; attenuation; sound velocity; finite difference; simulation

Citation: Duijster, A.; Volker, A.; Van den Berg, F.; Celada-Casero, C. Estimation of Grain Size and Composition in Steel Using Laser UltraSonics Simulations at Different Temperatures. *Appl. Sci.* **2023**, *13*, 1121. https://doi.org/10.3390/app13021121

Academic Editor: Sang-Hyo Kim

Received: 28 November 2022
Revised: 23 December 2022
Accepted: 27 December 2022
Published: 14 January 2023

1. Introduction

The mechanical properties of advanced high strength steels (AHSS) are greatly influenced by the grain size and the composition of the metallurgical phases. Both grain size refinement and the introduction or creation of secondary phases (e.g., martensite, bainite, pearlite) are mechanisms to strengthen AHSS. Hence, control of grain size, and control of secondary phase volume fraction are essential to master the mechanical properties. For consistent behavior of the product in forming processes, the mechanical properties, and hence the microstructure and composition, should remain constant. Therefore, real-time monitoring and control of the production process is important but challenging due to the harsh conditions. A potential way to measure the grain size and the secondary phase volume fraction in an inline manner during steel hot rolling is via laser ultrasonics (LUS). A complicating factor, however, is that the temperature varies during the process, affecting the ultrasonic properties as damping and wave velocity.

Since the proposal to use LUS as a new contactless measurement method for non-destructive testing of metals [1–5], the technology has been developed over the years to become a mature technology for a wide range of applications, such as corrosion monitoring [6], delamination detection in reinforced polymers [7], and in the determination of material properties [8–11]. Whereas in conventional transducer-based ultrasonic characterization a contact probe is used, LUS employs a laser pulse to generate an ultrasonic wave in the medium by ablating a small fraction of the sample material. The propagating ultrasonic

wave can be recorded by a measuring laser. The resulting measurement scheme is contactless, making it suitable for inline measurements in a steel mill, where the movement and temperature of the steel strip are a challenge for conventional transducers. Details on the physical background and practical applications of LUS techniques are described in several books and articles, e.g., [12–16]. Various LUS systems have been developed and used in offline systems [5,10,17–19] or as inline systems in steel mills [20].

Grain size and metallurgical composition are among the key factors determining material properties, such as strength, deformability, hardening and toughness, but also for detecting the formation of corrosion and pitting. Grain sizing. and time-varying aspects such as growth, deformation, recovery, and recrystallization have been studied in a variety of metals, such as manganese alloys [5], cobalt alloys [21], nickel alloys [9,22], aluminum [19,23] and stainless steels [24–27]. Monitoring of the metallurgical composition is especially important in dual phase (or multiphase) steels, where formability and strength depend on the phase ratio and phase distribution [28–32].

Efforts to model the ultrasonic wave propagation in materials with a microstructure have mainly focused on calculating attenuation and wave velocities in 3D, but backscattering has also been considered. Increasing computational power and the development of sophisticated computational methods such as finite difference (FD) or finite-difference time-domain (FDTD) methods [33,34] and finite element methods (FEM) [24,35–37], have enabled the modelling and computation of large three-dimensional samples. In these studies, materials with (poly)crystalline structures, consisting of different phases, or with inclusions, voids or cracks have been modelled.

Our investigation presents a model-based study to evaluate the capability of the LUS method to measure these grain size and metallurgical composition (apart from experimental measurement uncertainties). The study addressed the (inter-)dependencies of such a measurement, for example, to temperature. The literature (as mentioned before) has often provided insights in the relation between grain size or composition and various mechanical or (micro)structural properties, leading to a specific behavior of a material. However, the dependency on temperature fluctuation, and the effect of a temperature change on the estimation of grain size and phase composition, have not been studied extensively. The simulation setup enabled us to specify the properties of each grain independently, allowing for the generation of multiphase steels, temperature-dependent elastic properties, and texture.

Our analysis approach was to obtain the velocity and attenuation from simulations of ultrasonic wave propagation in various computer-generated (artificial) steel microstructures, at a range of temperatures. The research questions are:

1. How accurate can grain size be determined from LUS simulations on various simulated microstructures and temperatures?
2. How accurate can the phase composition be determined from LUS simulations on various multiphase media and temperatures?

Our studies were limited to modelling the ultrasonic wave propagation in the medium; the temperature dependency of the generation and detection of the waves by the laser were not considered, nor was the complex process of laser ablation.

2. Materials and Methods

2.1. Simulation Framework

Wave propagation in an elastic medium can be accurately and efficiently described using a finite-difference approach, which was the method followed in this study. Physical phenomena, such as mode conversion and frequency dependent scattering from grain boundaries, are included automatically. To calculate wave propagation, the elastodynamic equations are used, where the stresses and the particle velocities in the medium are described. Three sets of equations are required: the equation of motion, the strain-displacement equation, and the constitutive relation [38,39]. Note that the steel grains are modelled as anisotropic elastic media, thereby ignoring intrinsic damping mechanisms.

The numerical scheme that is used for the finite difference framework is based on a rotated staggered grid (RSG). Staggered grids are often used in finite-difference frameworks, which allows differences to be taken in a straight-forward way (parallel to one of the principal axes). However, they can lead to numerical artifacts in case of anisotropy, where differences over boundaries are not taken into account properly. In that case, an RSG provides better results. Saenger [39] applied the RSG to velocity-stress formulations of the elasto-dynamic wave equations. The advantage is that components are now located only at edges and in the center of an elementary cell, and not on the sides anymore.

A schematic process of the finite-difference simulation framework is depicted in Figure 1, from the source data (geometry, phase, and material properties; top left), via the individual grain (single crystal) elasticity constants to a 3D grid usable in the finite-difference simulation. The output of the simulation is the modelled measurement response of the microstructure to a specific excitation.

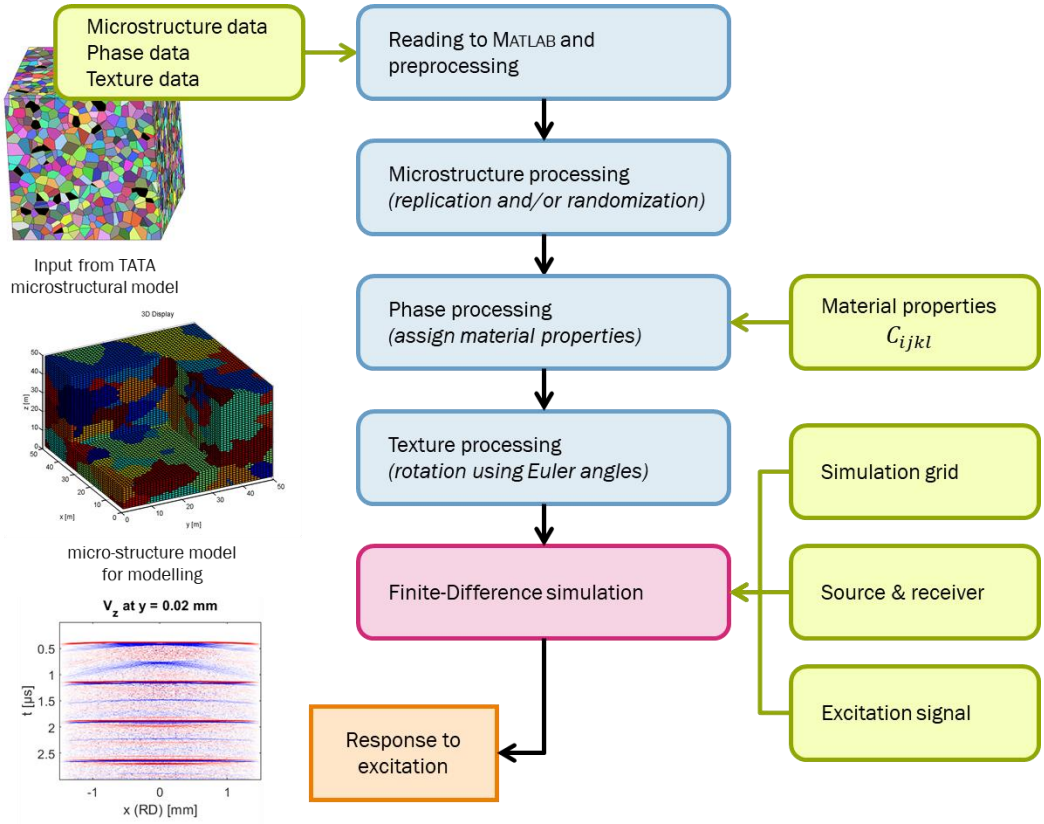

Figure 1. Schematic overview of the simulation process.

2.2. Fullsize Microstructures

Essential inputs for simulation are the properties of the sample, i.e., the grain structure, the phases of the individual grains and the texture. Periodic 3D microstructure models of relevant samples were digitally generated by Tata Steel in the form of a representative volume element (RVE) describing the location of individual grains [40]. The RVE generator, based on a multi-level Voronoi algorithm, is able to create periodic structures of up to 200,000 grains. Each grain is associated with a phase number and a set of three Bunge Euler angles describing the texture. The Bunge Euler angles are taken from the orientation distribution function (ODF) obtained from EBSD measurements. An ODF describes the distribution of Euler angles in the 3D Euler angle space. An example of such a microstructure is given in Figure 2. The size of a microstructural model is determined by the grain size and the used frequencies. With a maximum frequency of 60 MHz, a shear wave velocity of 3000 m/s, and at least 12 grid points per wavelength, the minimum grid size is 4.2 µm. In order to describe a wave appropriately, at least two sample points are needed

per grain. This means that a grid size of half the minimal grain diameter is needed (i.e., 2.5 µm for grains with diameter 5.0 µm). Based on these requirements, an integer grid size has been chosen and fixed to 3 micrometers. A grid size lower than this size, leads to a computationally much larger model (which scales to the power of four: three spatial dimensions and one temporal dimension).

Since the number of grains which can be handled by the microstructure generator software is bound to a maximum of 200,000 grains for periodic structures, the RVE samples cannot be generated at full size for FD simulation. Typically, the RVE sizes are in the order of $0.3 \times 0.3 \times 1.0$ mm, while the simulated sample is $3.0 \times 3.0 \times 2.0$ mm, which is 200 times larger. This limitation is overcome by replicating the original sample in all three Cartesian directions until the desired size has been obtained. This allows the generation of a much larger sample for FD simulation. However, replication of a sample leads to repetitive structures, which in turn lead to (strongly) amplified effects in ultrasonic wave propagation. The effect becomes more and more apparent as the replication number increases. Although it is unavoidable to obtain a repetitive microstructure (grain morphology), the texture can be randomized under the assumption that there is no spatial correlation between the texture of the individual grains. For each phase, the existing sets of three Euler angles are randomly redistributed over all grains belonging to that phase, keeping the sets themselves intact (and thus preserving the texture), and keeping the sets bound to their specific phase (no cross-over of texture between phases). As a result, the texture is not repetitive anymore, although the microstructure remains periodic. This process is illustrated in Figure 3.

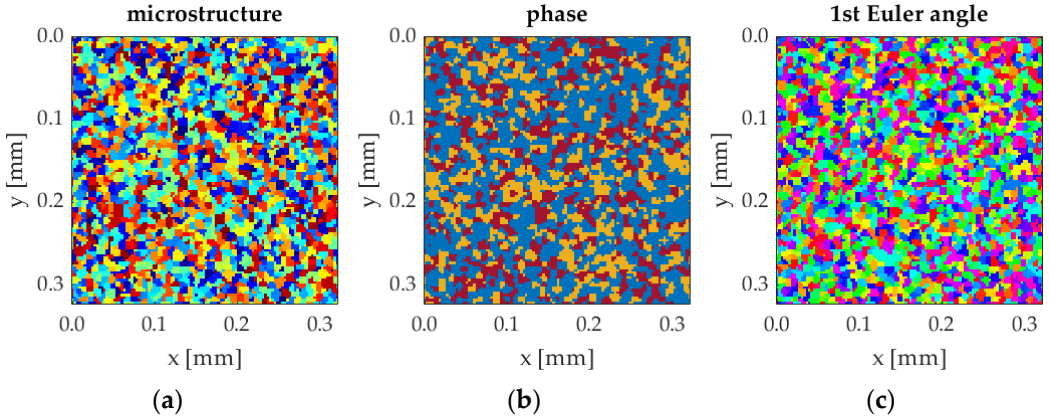

Figure 2. A 2D cross-section of: (**a**) a microstructure; (**b**) the corresponding three phases; and (**c**) the first of three Bunge Euler angles. The colors in (**a**) refer to a grain number, the colors in (**b**) refer to the phase, and the color scale in (**c**) is related to an angle between 0 and 2π.

An essential aspect in the interaction of ultrasonic waves and microstructure is grain scattering. The physical background behind grain scattering is the contrast between two adjacent grains, which causes a part of the incoming wave to be scattering instead of being transmitted. The level of grain scattering in a material depends on one hand on the size of the grains, and on the other hand on the contrast in the elastic properties. The contrast itself depends on the texture (crystal alignments, determined by a set of Bunge Euler angles, with respect to the RVE frame) and on the physical properties of the grain (crystal properties, determined by its material and phase). Modelling grain scattering hence requires the grain morphologies, the grain material (phase) and its single crystal properties, and the texture.

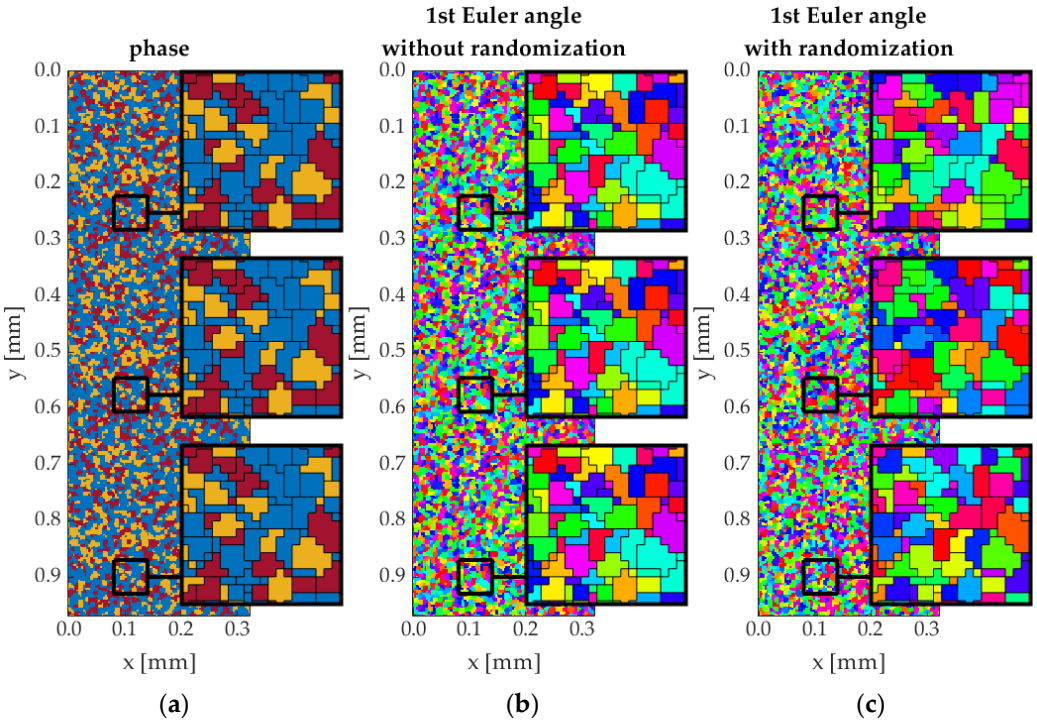

Figure 3. An example of replication and randomization. On the left (**a**), the phase is shown, replicated three times in *y*-direction. The middle image (**b**) shows an ordinary replication of the first Bunge Euler angle. Note the repetitive patterns in the zooms. The image on the right (**c**) shows the results of Euler angle randomization per phase after replication, which eliminates the repetitive pattern in the texture. After randomization, the phases corresponding with (**c**) still remaining the same as in (**a**). The colors are corresponding with those used in Figure 2.

A set of RVEs were generated with one or two different phases, varying phase ratios (in steps of 25%), and/or varying grain sizes (5, 10, 15 or 20 µm in diameter). This grain size range is typically expected in steel during processing in the hot strip mill. In the computer-generated microstructures, different phases were indicated by a different identifier. The actual physical properties of a phase were attributed only upon the ultrasonic wave simulation. This procedure allowed the reuse of the same morphologies for simulations with different phase constituents.

2.3. Temperature-Dependent Material Properties

In the generation of an RVE, each grain is assigned to a phase. In Figure 2b an example is shown for a sample with three phases. From the literature, a series of single crystal properties can be obtained, as shown in Table 1 in Voigt notation. In general, these elastic constants are computed from measurements to wave velocities, or strains and stresses. The values of ferrite are very close (differences less than 1.5%) and those of austenite differ up to 5%. This may indicate that the assumed temperatures might be off.

Table 1. Single crystal properties found in literature.

		Material				
		Ferrite [41,42]	**Ferrite [43]**	**Martensite [44]**	**Austenite [45,46]**	**Austenite [47]**
Elastic constants [GPa]	C_{11}	233.1	231.5	237	198	192.7
	C_{22}	233.1	231.5	237	198	192.7
	C_{33}	233.1	231.5	256	198	192.7
	C_{23}	135.4	135.0	144	125	131.3
	C_{13}	135.4	135.0	144	125	131.3
	C_{12}	135.4	135.0	144	125	131.3
	C_{44}	117.8	116.0	115	122	126.3
	C_{55}	117.8	116.0	115	122	126.3
	C_{66}	117.8	116.0	115	122	126.3
Zener's anisotropy	$\mathcal{Z}$	2.41	2.40	2.47	3.34	4.11
Reference temperature	T_{REF}	300 K (27 °C)	room temperature	0 K (−273 °C)	not mentioned, assumed 298 K (25 °C)	not mentioned, assumed 298 K (25 °C)

A dimensionless metric that describes the anisotropy of a crystal, known the Zener ratio or Zener's anisotropy, has been defined for cubic crystals [44,48] as

$$\mathcal{Z} = \frac{2C_{44}}{C_{11} - C_{12}}. \tag{1}$$

The ratio is (close to) 1 for isotropic media. The isotropy of the crystalline materials is also listed in Table 1.

The elastic properties of steel depend on the temperature, as has been shown e.g., by Ghosh [41]. Based on GLUS® measurements (method described in [13,49]) and data inversion [50], the temperature dependencies of the aforementioned material types have been obtained.

The elastic constants $C_{ij}(T)$ were experimentally determined for each material in Table 1 at a discrete number of different temperatures. A polynomial function was fitted to this data to obtain the temperature dependency. The temperature dependency was modelled as

$$C_{ij}(T) = \left(a_{1,ij}T^2 + a_{2,ij}T + 1\right)C_{ij}(T_{\mathrm{REF}}), \tag{2}$$

where $C_{ij}(T_{\mathrm{REF}})$ is the elastic constant C_{ij} at the reference temperature T_{REF} (also listed in Table 1), T is the temperature in the simulation, and $\begin{bmatrix} a_{1,ij} & a_{2,ij} \end{bmatrix}$ are the experimentally determined polynomial coefficients. In the simulations, the required elastic constants of a material at a specific temperature were obtained by entering the constants at the reference temperature (from Table 1) and the polynomial coefficients into Equation (2).

An example is shown in Figure 4a, where the temperature dependency of the elastic coefficients C_{11}, C_{12}, and C_{44} is plotted. The curve is determined based on the aforementioned measurements in the range between 100 °C and 500 °C, but extrapolated values down to −273 °C are also plotted as a dotted line. The experimental values which Ghosh lists in his article [41] (originally measured by Rayne [42]) are shown as well. Although there are deviations between Ghosh's values and the curve, the trends are comparable. Temperature dependencies of other phases have not been found in the literature but based on the match between the extrapolated experimental results and Ghosh's results, the approach is considered to be valid.

Note that the temperature dependency of the elasticity matrix is different for each component, both in absolute and in relative sense. For ferrite, the C_{12} shows a much smaller relative decrease than C_{11}, which has in turn a smaller relative decrease than C_{44}. The

ratio of their decrease determines the single crystal isotropy and the behavior at higher temperatures, influencing the wave velocity and attenuation.

In addition to the elasticity matrix, the density also depends on the temperature. Values for ferrite, martensite and austenite are taken from papers from Cho and Lyassami [51,52]. The resulting densities as a function of temperature are shown in Figure 4c.

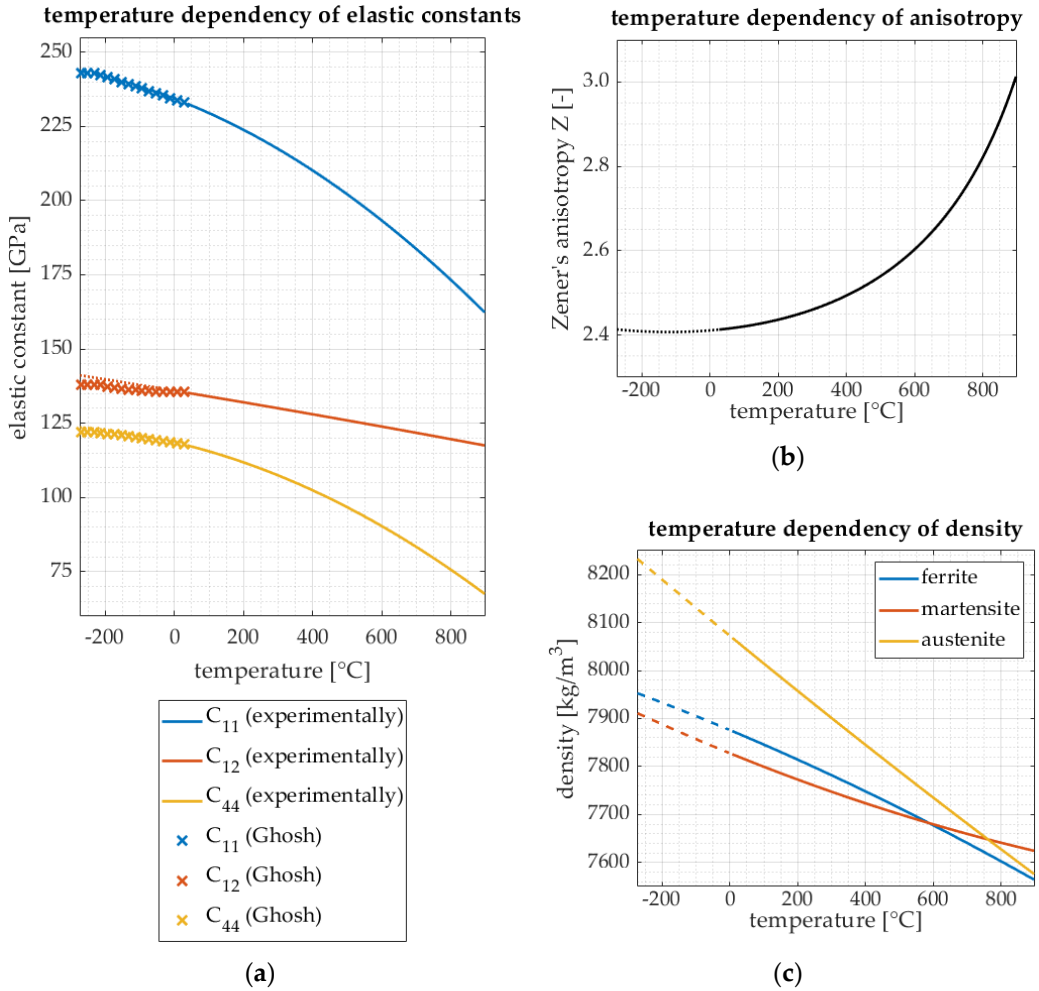

Figure 4. (**a**) The elastic coefficients C_{11}, C_{12}, and C_{44} of ferrite plotted as function of temperature between room temperature and 900 °C as a solid line. An extrapolation down to the absolute minimum temperature is shown as a dotted line. Values as given by Ghosh [41] are shown as crosses; (**b**) the isotropy $\mathcal{Z}$ as derived from the temperature-dependent elasticity coefficients; and (**c**) the temperature-dependent densities of ferrite, martensite and of austenite [51,52].

2.4. LUS Modelling, Data Processing and Analysis

The characterization of grain sizes and phase variations can be achieved by analysis of the propagation of high-frequency ultrasonic waves in a LUS setup. Samples of 3.0 × 3.0 × 2.0 mm (length × width × height) have been used with a spatial resolution of 3.0 µm. This sample size is restricted due to practical limitations regarding computer memory use and computation time.

For LUS, a relatively large source has been defined, with a flat top and smoothened sides, as shown in Figure 5. The full width at half maximum (FWHM) is 1.5 mm, while the flat top is roughly 0.75 mm in diameter. Note that the size is limited by the sample size, which in turn is limited by computational capabilities.

The full bottom of the sample has been recorded throughout the simulation. A receiver is defined with the same size as the source, but on the bottom side of the sample.

The excitation signal is a single pulse with a center frequency of 25 MHz and a bandwidth of 64 MHz (at −20 dB), as shown in Figure 6, inducing a vertical compressional wave. The design of the spot size was optimized for grain size measurement, for texture measurement a much smaller spot size should be used.

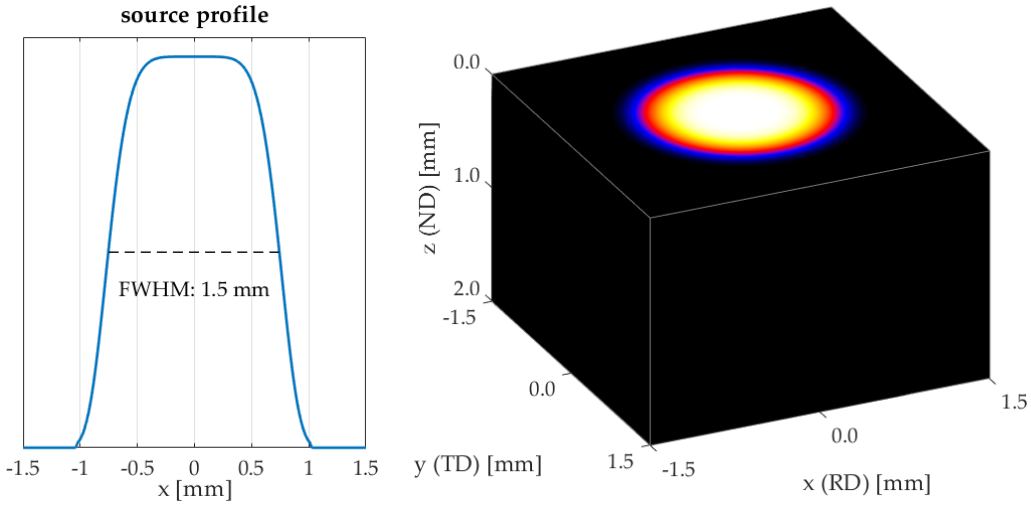

Figure 5. (**a**) The source profile in 1D; and (**b**) the source at the top the sample in 2D.

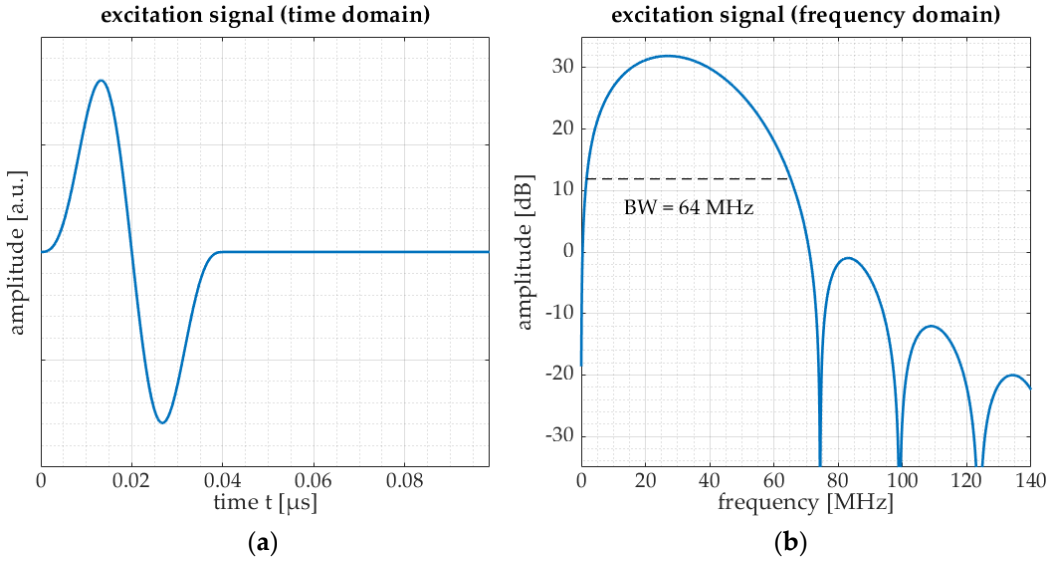

Figure 6. (**a**) The excitation signal (**a**) in the time domain; and (**b**) in the frequency domain. The dashed line denotes the bandwidth at −20 dB.

The signal was recorded at the bottom of the sample for a duration long enough to capture the primary wave and five or six passes through the thickness of the sample. Since the source was relatively large, the wave travelling up and down in the sample was regarded as a plane wave. Two cross-sections of a recording are shown in Figure 7, respectively, a recorder line at the bottom at y = 0 mm, and a single recorder point at $(x, y) = (0, 0)$ mm. The receiver accumulates the signal from the bottom surface with radius $r = 2.1$ mm. This leads to spatial averaging of the grain scatter noise, while maintaining the shape of the plane wave.

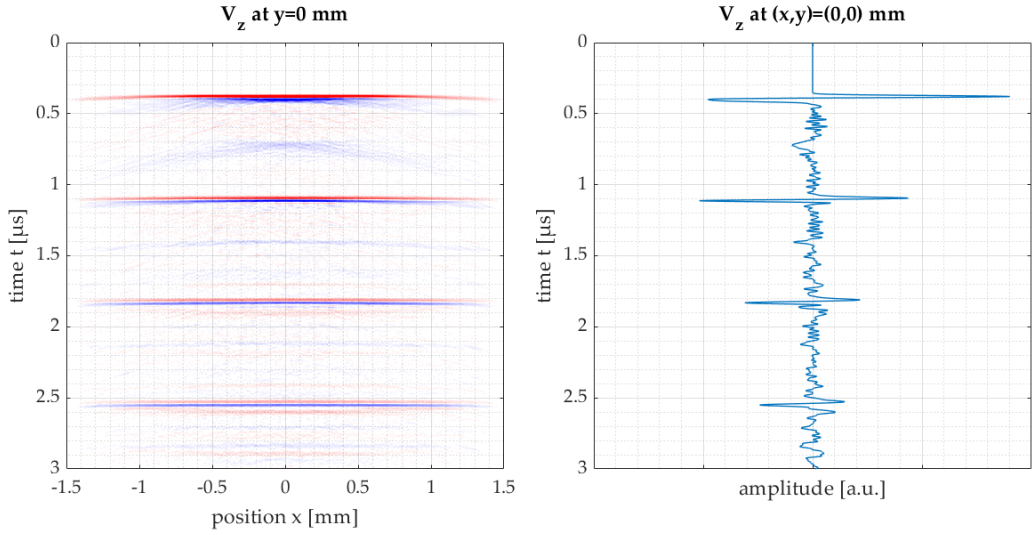

Figure 7. A cross-section of a recording (**a**) along a line (red colors denote a positive signal and blue a negative); and (**b**) from a single receiver in the center.

The recorded signal shows a series of pulses. Those pulses are the primary compressional wave and internal reflections of the compressional wave. The smaller events in between the main pulses are mode conversions and noise due to grain scattering. As can be seen, the amplitude of the pulses decreases over time due to the mode conversion, energy spreading horizontally in the plate and grain scattering. Keyvani mentions three main contributors to the attenuation of an ultrasound pulse in a medium with a microstructure [21]:

1. Grain scattering, leading to wave energy dispersion due to mismatches in elasticity in neighboring grains (crystallographic orientation differences due to texture);
2. Diffraction of the ultrasonic wave in the medium, affecting both the frequency content as well as the amplitude;
3. Absorption of wave energy, which is assumed to be of minor importance to frequency-dependent attenuation.

The first two aspects were incorporated in the finite-difference simulations; the third was not, but according to Keyvani, this would have had a negligible effect on the results.

The wave velocity c can be determined by measuring the delay Δt between the arrival of pulses and the thickness of the sample H, as

$$c = 2H/\Delta t. \tag{3}$$

The factor 2 is due to the fact that the wave travels up and down through the sample in between two pulses. The wavelength λ corresponding to frequency f is given by

$$\lambda = c/f. \tag{4}$$

Due to grain scattering the spectral content of each pulse changes. Higher frequencies are more attenuated due to grain scattering than lower frequencies. This can be seen in Figure 8, where the weighted average frequency decreases for each subsequent echo. Note that this attenuation also heavily depends on the average grain sizes of the material.

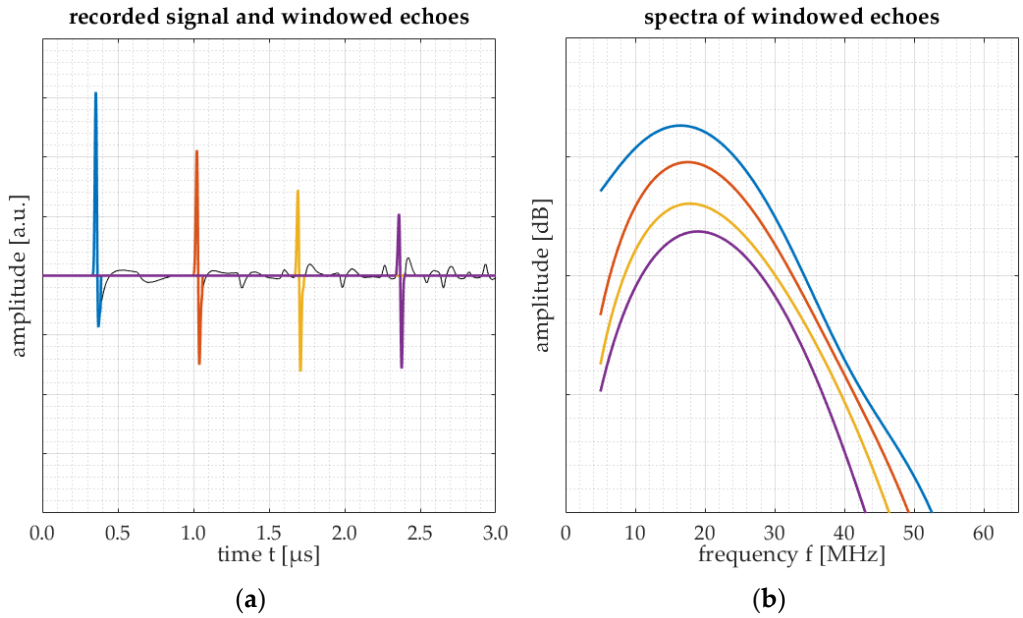

Figure 8. (**a**) The windowed echoes in the time domain; and (**b**) their corresponding spectra in the frequency domain. The four colors correspond in both subplots.

In general, three grain scattering regimes are considered, depending on the ratio of wavelength and grain size [24,53]:

1. The Rayleigh regime, where $\lambda \gg d$, leading to an attenuation coefficient $\alpha \sim d^3 f^4$;
2. The stochastic regime, where $\lambda \approx d$, leading to an attenuation coefficient $\alpha \sim d f^2$; and
3. The diffusion or geometric regime, where $\lambda \ll d$, leading to an attenuation coefficient $\alpha \sim d^{-1}$.

The attenuation coefficient over all these regions can be generalized to $\alpha \sim d^{\gamma-1} f^{\gamma}$, covering all three regions and bridging the gaps in between. An illustration of the ratio between grain diameter and frequency is shown in Figure 9.

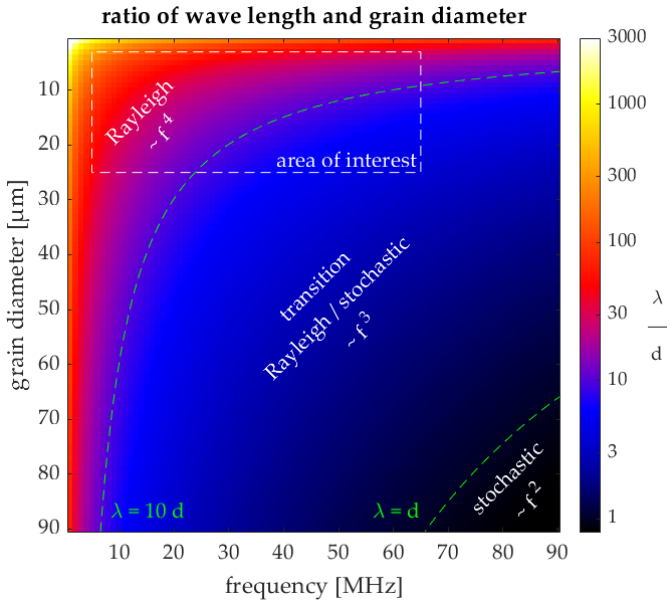

Figure 9. The Rayleigh and stochastic scattering regimes and the transition regime in between. The box on the upper left is the area of interest, bound by the used frequencies and the modelled grain sizes.

For typical velocities of 5750 m/s and frequencies between 5 and 50 MHz, the wave lengths are between 1.2 and 0.12 mm respectively. Compared to the considered grain sizes, 5 to 20 µm, the wave lengths are (much) larger, indicating that the Rayleigh scattering regime is mostly applicable here, but close to the stochastic regime, with an expected attenuation coefficient $\alpha \sim f^{\gamma}$ with $3 \leq \gamma \leq 4$.

The frequency-dependent attenuation can be obtained in two ways, as described by Keyvani [21]:

1. Compare two echoes of a single measurement, where one echo has travelled a longer distance through the medium than the other and hence has undergone more attenuation due to the medium's microstructure;
2. Compare two echoes from two different measurements (both the same echo number), of which one originates from a well-known medium and the other from the medium to be characterized. Assumed is that the media have the same thickness and hence the waves have travelled the same distance.

Following the second approach of Keyvani, i.e., comparing echoes from two different measurements, the frequency-dependent attenuation $\alpha_{n,m}(f)$ of sample n for echo m is obtained as

$$\alpha_{n,m}(f) = \frac{20}{(2m-1)H} \log_{10} \frac{|S_{\mathrm{REF},m}(f)|}{S_{n,m}(f)}. \tag{5}$$

where H is the sample thickness and hence $(2m-1)H$ corresponds with the total travelled distance of the signal providing echo m. $S_{\mathrm{REF},m}$ and $S_{n,m}$ are the spectra of the reference sample and the sample to be analysed, respectively.

Echo 1 is the primary wave, which has travelled only once through the sample. As a result, the influence of scattering and attenuation on this echo is not very pronounced. The second echo has travelled three times through the sample and each next echo adds two more passes compared with the previous one. Due to the limited path length, the first echo is left out in further analysis, and only the second, third and fourth echoes are used, hence $m \in [2, 3, 4]$. Echoes 5 and beyond are not considered, since the signal (echo) to noise (scattering) ratio for those echoes decreases too drastically, especially for samples with larger grain sizes. The attenuation for the given simulation example, compared to a reference sample (here taken as the same material, but with a slightly larger grain size), is computed and shown in Figure 10 for echoes 2, 3 and 4. Both $\gamma = 3$ and $\gamma = 4$ show a reasonable fit in the considered frequency range, although an optimal value for γ might be in between 3 and 4. Note that the frequency range depends on the echo: up to 55 MHz for echo 2, up to 48 MHz for echo 3 and up to 41 MHz for echo 4. For higher order echoes, scattering and interference of mode conversions becomes more apparent in the less smooth curves. Additionally, the low SNR limits the upper boundary of the frequency range which can be used for the fitting. In order to be able to use a large frequency range, the second echo was chosen for further processing.

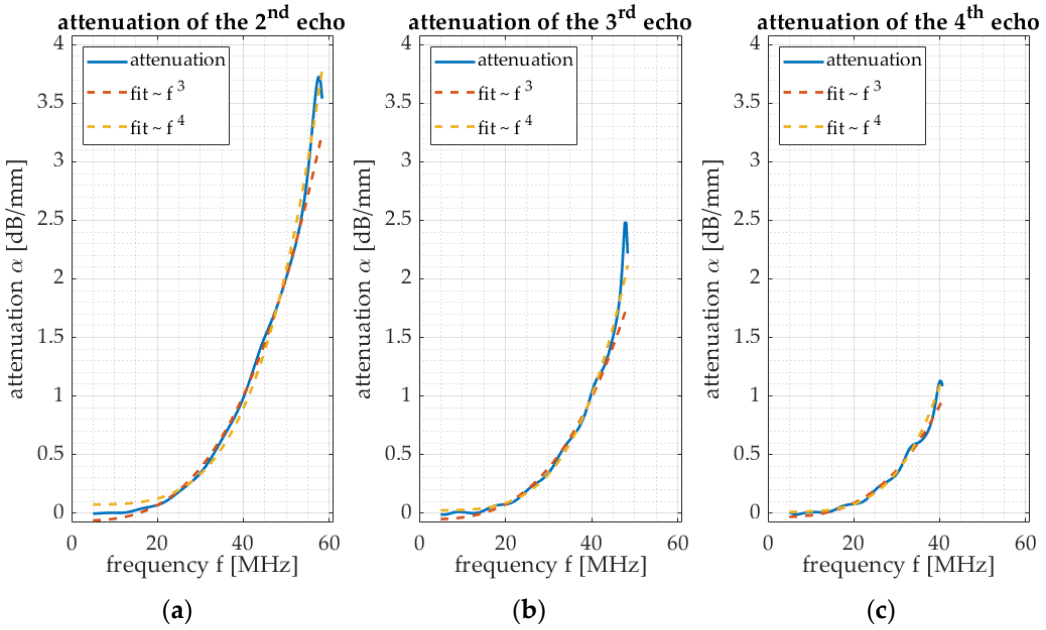

Figure 10. The attenuation curves of respectively (**a**) the second echo; (**b**) the third echo; and (**c**) the fourth echo normalized to a reference sample. For each curve, two polynomial fits $\alpha = a + bf^{\gamma}$ are overlaid for both $\gamma = 3$ and $\gamma = 4$.

The choice of a fixed exponent for the fits is always an approximation, since the attenuation $\alpha(d, f) \sim d^{\gamma-1} f^{\gamma}$ depends both on the grain size d (which might vary in between simulations, but is in the order of 5 to 20 µm) and frequency f (which covers a range between 5 and 60 MHz in each simulation).

The scattering is considered to be in the Rayleigh regime ($\gamma = 4$) and in the transition regime ($\gamma = 3$), as can be seen from the area of interest in Figure 9. Since several experimental systems use a constant exponent $\gamma = 3$ [5,20,21,54], this same exponent has been chosen here as a compromise. This constant exponent $\gamma = 3$ has been used for the whole range of grain sizes.

After obtaining the attenuation $\alpha(f)$ a function $\hat{\alpha}(f) = a + bf^3$ is fitted, and the parameter b is determined. A new parameter

$$b' = \begin{cases} \sqrt{|1000 \cdot b|} & \text{for } b \geq 0 \\ -\sqrt{|1000 \cdot b|} & \text{for } b < 0 \end{cases}. \tag{6}$$

is defined, based on [20,21]. Note that the signs of b and b' are the same, enabling a distinction between a positive and negative b.

3. Results

A set of ten samples was simulated at four different temperatures, ranging from 27 °C up to 900 °C, and containing various phases, as shown in Table 2. The selected temperature range matched with the temperatures met during the last stages of hot rolling and during continuous annealing in steel manufacturing. The set of phase compositions were chosen as a rigid matrix to obtain a straightforward comparison and simple trend lines; however, the reader should be aware that certain combinations of phases, grain sizes and temperatures will not occur in practice. From this full set of simulations, particular subsets can be taken to study individual effects as grain size or phase variation:

A. The effect of grain size on the 100% austenite samples;
B. The effect of grain size on the 100% ferrite samples;
C. The effect of phase variation on the austenite/martensite samples;
D. The effect of temperature on all samples.

The last column of the table shows which simulations are used for these four subsets. Note that, in reality, some of these steel phases do not exist at the simulated temperatures, but they are taken into account to study trends and dependencies.

Table 2. Ten simulation cases for LUS simulations. Each case has been simulated at temperatures of 27 °C, 300 °C, 550 °C, and 900 °C. The subset IDs refer to the four cases in Section 3.

Microstructure Geometry ID	Average Grain Diameter [µm]	Material Properties (Phases and Phase Ratios)	Subset IDs
1	10.0	100% Austenite	A, D
2	15.0	100% Austenite	A, C, D
3	20.0	100% Austenite	A, D
4	5.4	100% Ferrite	B, D
5	10.0	100% Ferrite	B, D
6	15.0	100% Ferrite	B, D
7	A: 15.0, M: 10.0	75% Austenite, 25% Martensite	C, D
8	A: 15.0, M: 10.0	50% Austenite, 50% Martensite	C, D
9	A: 15.0, M: 10.0	25% Austenite, 75% Martensite	C, D
10	10.0	100% Martensite	C, D

3.1. Microstructure

Two subsets of the performed simulations were taken for analysis: a series of austenite samples with increasing grain diameters, and a comparable set of ferrite samples with three different grain diameters. These are the series A and B from Table 2. Grain diameters are estimated from the data, ignoring the truncated grains at the edges. Assuming spherical grains, an average grain diameter $\hat{D}$ can be deduced from the average grain volume $\hat{V}$ as

$$\hat{D} = \sqrt[3]{\frac{6\hat{V}}{\pi}}. \tag{7}$$

The grain diameters retrieved from the austenitic steel samples are 10.0, 15.0 and 20.0 µm, while the ferritic samples have diameters of 5.4, 10.0 and 15.0 µm, respectively. For each of those six samples, simulations have been performed at four different temperatures (27 °C, 300 °C, 550 °C, and 900 °C). These temperatures have been used in the simulations to study the same temperature domain for ferrite and austenite. Note that the phase transition temperature has not been taken into account, and that some of these (pure) steel phases do not actually exist at the chosen temperatures.

Per set, the underlying microstructures only differ in grain size. The texture is isotropic in all samples. The variation in between the average elasticity matrices of the three samples within each set, is less than 0.1%, taken from samples at the same temperature. For the pure polycrystalline materials austenite, ferrite and martensite, the corresponding Voigt-Reuss-Hill averages [55] of the elasticity matrices at 27 °C are shown in Figure 11. Zener's anisotropy metric $\mathcal{Z}$, as defined in Equation (1), of all three samples is 1.000, which indicates perfect isotropy.

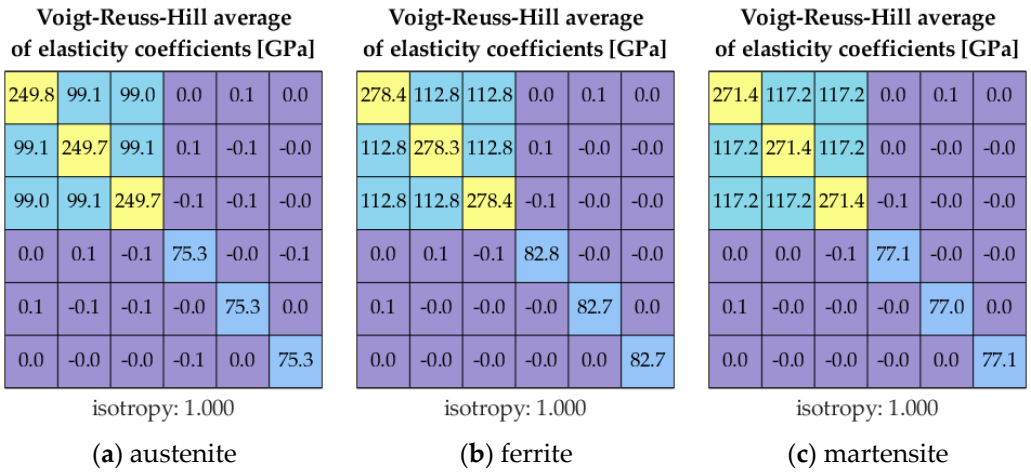

Figure 11. (**a**) The Voigt-Reuss-Hill averaged elasticity matrix of the samples of (**a**) pure austenite; (**b**) pure ferrite; and (**c**) pure martensite. All values are obtained from samples at a temperature of 27 °C. The elasticity matrices are independent of the grain size.

The wave propagation velocity can be determined as a function of the temperature by finding the time delay between two consecutive echoes. By dividing the travelled distance $2H$ (i.e., double the sample thickness) by this time delay Δt, the velocity c is obtained, as in Equation (3). Results are shown in Figures 12 and 13, where the observed velocities are plotted either as function of grain diameter or as a function of temperature.

As can be seen, the temperature has a significant effect on the wave velocity. This is due to the strong temperature dependencies of both the elasticity matrix and the density. Note that the individual components of the elasticity matrix and the density are nonlinearly dependent of the temperature, as can be seen in Figure 4, leading to nonlinear velocity curves in Figure 13. On the other hand, the grain size variation has a much smaller impact on the wave velocity than temperature. Grain size affects the wave velocity due to small time delays induced by scattering of waves, leading to relatively small changes in the resulting wave velocity. The larger the grains, the greater the delay caused by multiple scattering and hence the lower the resulting wave velocity.

Hence it can be concluded that the wave velocity itself cannot be used effectively to estimate the grain size due to its small sensitivity to grain size and its much larger temperature dependency. For a pure austenitic sample, an increase in grain size of 1 µm means a velocity decrease of 1.6 m/s (Figure 12a), and for a pure ferritic steel this value is 1.1 m/s per µm (Figure 12b). However, the same velocity decrease can also be caused by several other parameters, e.g., a temperature increase in the order of 1 to 2 °C (Figure 13a,b) or a small change in sample thickness (in the order of micrometers). In order to be able to determine such small velocity differences, parameters such as temperature and also sample thickness must be measured very accurately, rendering this method unfeasible for the determination of grain size.

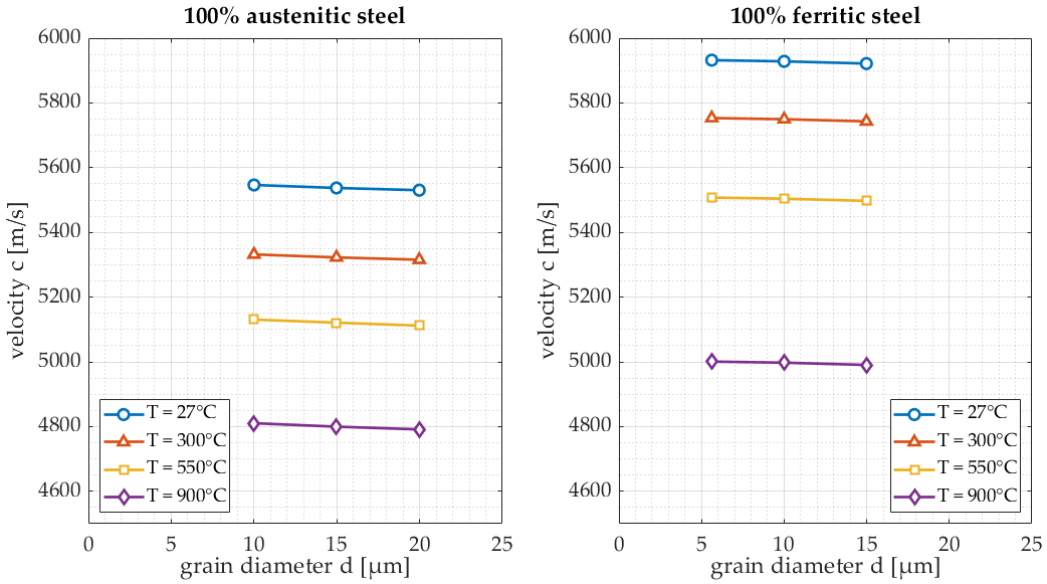

Figure 12. The relation between the grain diameter d, and observed wave velocity c for two material types and four temperatures: (**a**) shows 100% austenitic steel; and (**b**) 100% ferritic steel.

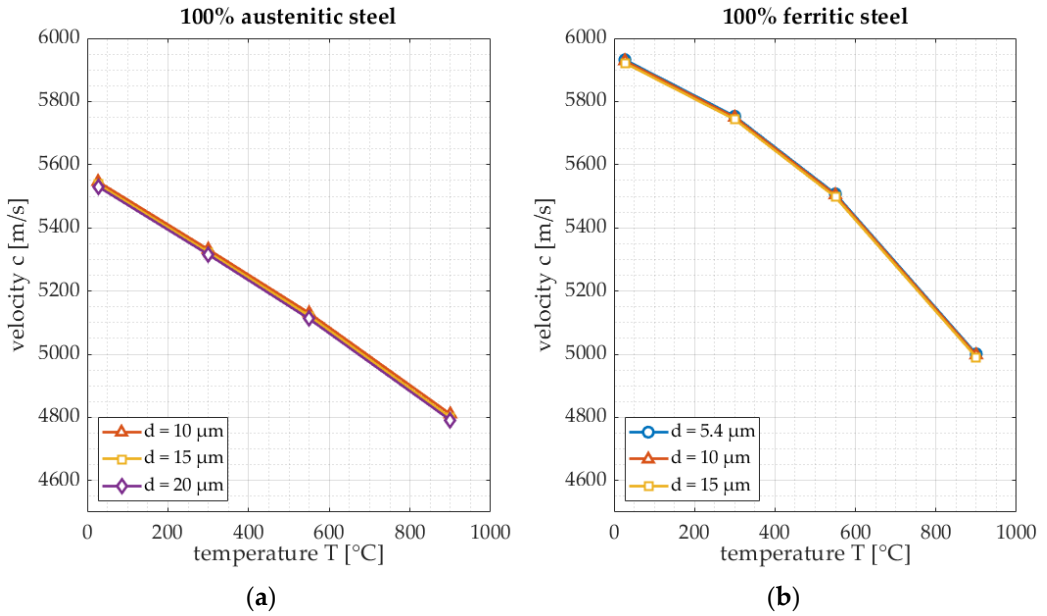

Figure 13. The relation between the temperature T, and observed wave velocity c for two material types and three grain sizes: (**a**) shows 100% austenitic steel; and (**b**) 100% ferritic steel.

Simulations of other microstructure realizations or randomizations (pure austenite, grain size 15 µm, at 300 °C) lead to velocity variations less than ±0.4 m/s. This relates to a grain size variation up to 0.2 µm, which does not have a significant impact on grain sizing.

Results of the attenuation analysis are shown in Figures 14 and 15, where the results of the fit to the attenuation of the second echo has been plotted, in terms of b', as defined in Equation (6). For each of the constant temperature series in Figure 14, the sample with the middle grain size has been used as the reference sample. Hence, the corresponding data points all coincide at $b' = 0$ for martensite at $d = 15$ µm and for ferrite at $d = 10$ µm. Similarly, as a reference sample in Figure 15, the sample with temperature $T = 300$ °C has been used for each of the grain sizes.

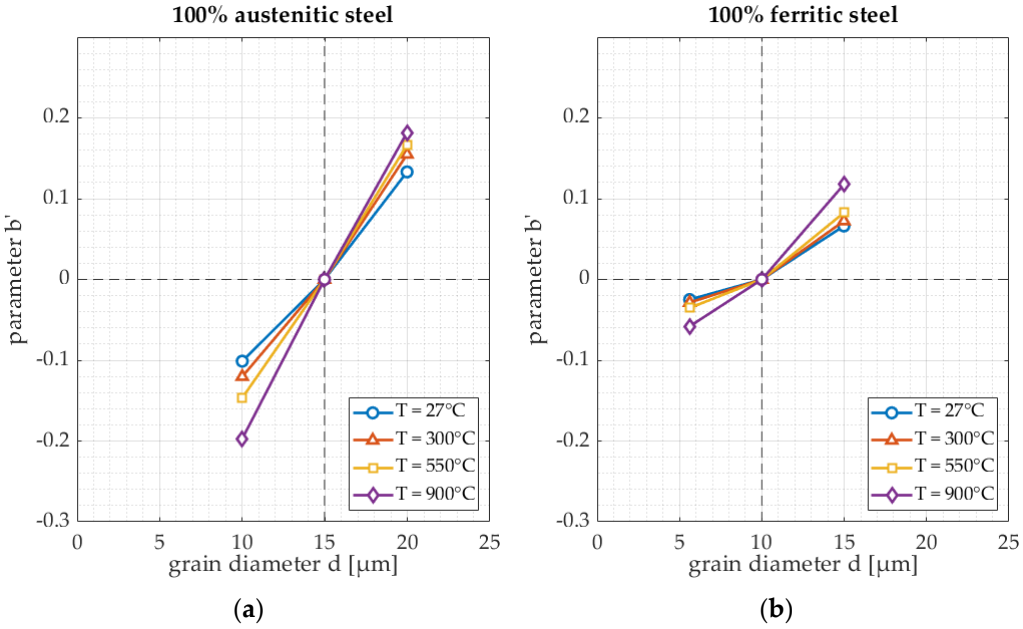

Figure 14. The relation between the grain diameter d, and parameter b' for two material types and four temperatures: (**a**) shows 100% austenitic steel; and (**b**) 100% ferritic steel.

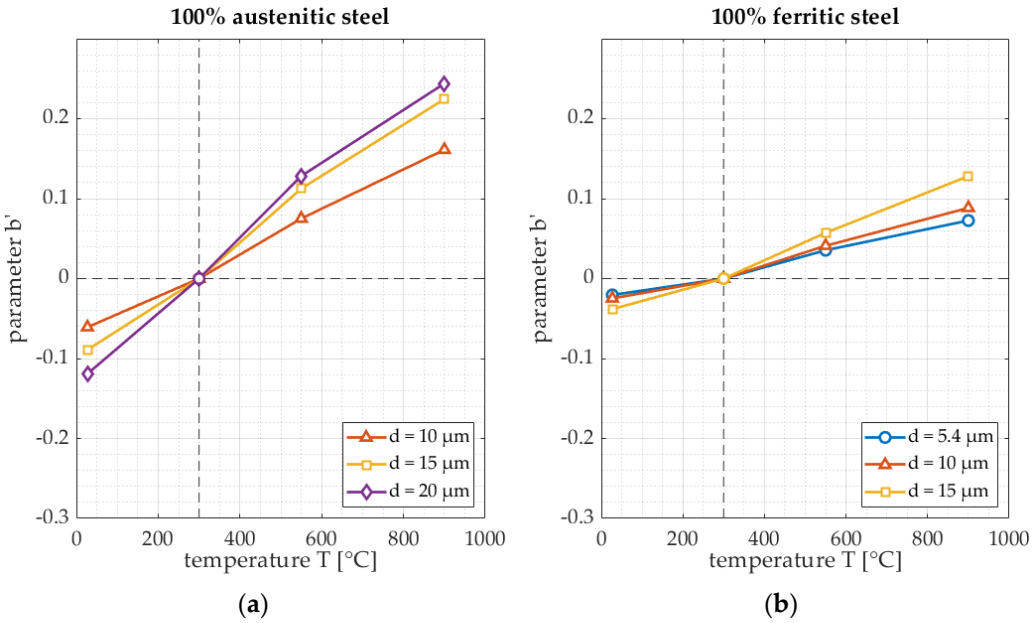

Figure 15. The relation between the temperature T, and parameter b' for two material types and three diameters: (**a**) shows 100% austenitic steel; and (**b**) 100% ferritic steel.

The curves, both as function of grain size and temperature, appear to be approximately linear for pure austenite and pure ferrite, as far as can be determined with only three or four data points per curve, which is in accordance with Wan [24]. A generic quantitative relationship cannot be properly determined. Note that the attenuation parameter for ferrite is a bit higher than expected for the smallest grain size (grain size less than 10 µm, Figure 14b). It is assumed that this may be due to the fact that the wave propagation in the small grains of these samples is prone to computational errors: since there are less than 2 grid points per average grain, the results are assumed to be less reliable.

The curves show slopes which depend on both grain size and temperature. Hence, a change in attenuation can be attributed to a change in grain size, in temperature or

in a combination of both. Knowing the sample temperature sufficiently accurate and using a curve corresponding with this temperature is essential to avoid sizing errors. A simultaneous measurement of the wave velocity to estimate the temperature (according to Figure 12) may be used for such temperature correction.

A grain size increase of 1 μm leads to an increased attenuation b' of 0.03 (pure austenite, 15 μm at 300 °C, Figure 14a). A temperature change of 10 °C causes an attenuation change in the order of 0.004 (pure austenite, 15 μm at 300 °C, Figure 15a), which is one order of a magnitude lower. This shows that an effect of temperature is present, but much less prominent than in the velocity measurements. For ferrite, the slopes are not as large as for austenite, indicating that grain size estimation from attenuation will be less accurate. Here, the attenuation value is 0.011 per μm (pure ferrite, 10 μm at 300 °C, Figure 14b), which is also some ten times larger than the attenuation change caused by a temperature increase of 10 °C: 0.0013 (pure ferrite, 10 μm at 300 °C, Figure 15b). Hence, estimation of grain size in the order of 1 μm based on the attenuation requires measurement of the attenuation in the order of a few hundredths, and measurement of the temperature in the order of 10 °C, which is feasible.

The velocity computation is very sensitive to sample thickness, as can be seen in Equation (3). The attenuation is expected to be less sensitive to sample thickness variation, since it is based on the comparison of two signal spectra. The spectra themselves depend on the travelled distance (which in turn directly relates to the sample thickness), but they vary only slightly with thickness variations. Simulations with slightly varying thicknesses have not been performed, rendering it impossible to quantify the effect of thickness variation on attenuation and to present constraints.

Simulations of other microstructure realizations or randomizations (pure austenite, grain size 15 μm, at 300 °C) lead to attenuation variations less than ±0.009. That variation corresponds with a grain size variation of less than 0.3 μm. This indicates that variation in morphologies and Euler angle distributions does not have a significant impact on grain sizing.

3.2. Multiphase

A set of simulations has been performed on samples with various ratios of austenite and martensite as material. This is the series marked with 'C' in Table 2. The grain diameters are the same in all five samples: 10.0 μm for martensite and 15.0 μm for austenite. For each of those samples, simulations have again been performed at four different temperatures (27 °C, 300 °C, 550 °C, and 900 °C). These temperatures were used in the simulations to study a large temperature domain. Note that again the phase transition temperature has not been taken into account and that this multiphase steel might not actually exist at all four simulated temperatures.

The elasticity coefficients (based on the polycrystalline Voigt-Reuss-Hill average) of the sample are shown in Figure 16, as well as the isotropy. As can be seen, all samples are nearly isotropic, and the coefficients show a (nearly) linear relation with the phase ratio (in terms of percentage martensite). The given values are for a temperature of 550 °C, but other temperatures show the same trends.

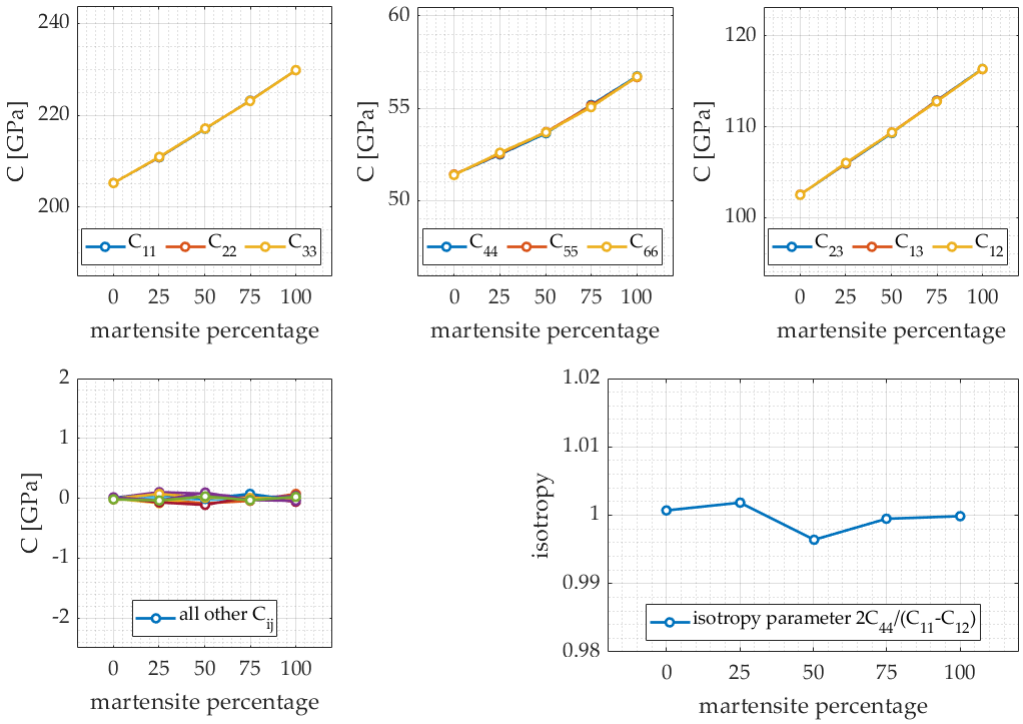

Figure 16. All polycrystal (Voigt-Reuss-Hill averaged) coefficients plotted as function of the phase ratio (in percentage of martensite, with the other phase being austenite). The bottom right curve shows the isotropy $\mathcal{Z}$ (cf. Equation (1)) in all five samples for a temperature of 550 °C.

The observed wave velocities for the five samples and four temperatures are shown in Figure 17, which show linear trends as function of the phase ratio. Although the grain size of the individual phases is kept invariant in all simulations, the average grain size of the total sample increases with the amount of austenite. However, since the scattering is only of minor impact on the wave velocity (cf. Figure 12), the underlying elasticity matrices are expected to be the dominant determining factor for the wave velocity. The resulting relation is linear with the phase ratio. However, the relation with temperature (Figure 17b) depends on the underlying material properties, which reveals its non-linearity.

Differences in wave velocity are relatively small (in the order of 3.7 m/s difference for each percent in phase ratio difference (50% martensite at 300 °C, Figure 17a). Measurement of such small differences (5 m/s means a change in the order of 0.1% of the total velocity) means the sample thickness has to be measured at least as accurate (order of micrometers), which is very challenging. At the same time, the temperature has to be known accurately as well, since a 4 °C temperature increase can also lead to a 4 m/s velocity decrease (50% martensite at 300 °C, Figure 17b). As in the previous case of grain sizes, the propagation wave velocity measurement is also not a viable method for phase ratio characterization.

Results of the attenuation analysis are shown in Figure 18. As a reference, the sample with 50% martensite and 50% austenite is taken in subplot a) and the sample with a temperature of 300 °C in subplot b). With only five different ratios, the curves appear not very smooth, although a trend is visible. Given this limited set of simulations, it is hard to derive a reliable quantitative relationship.

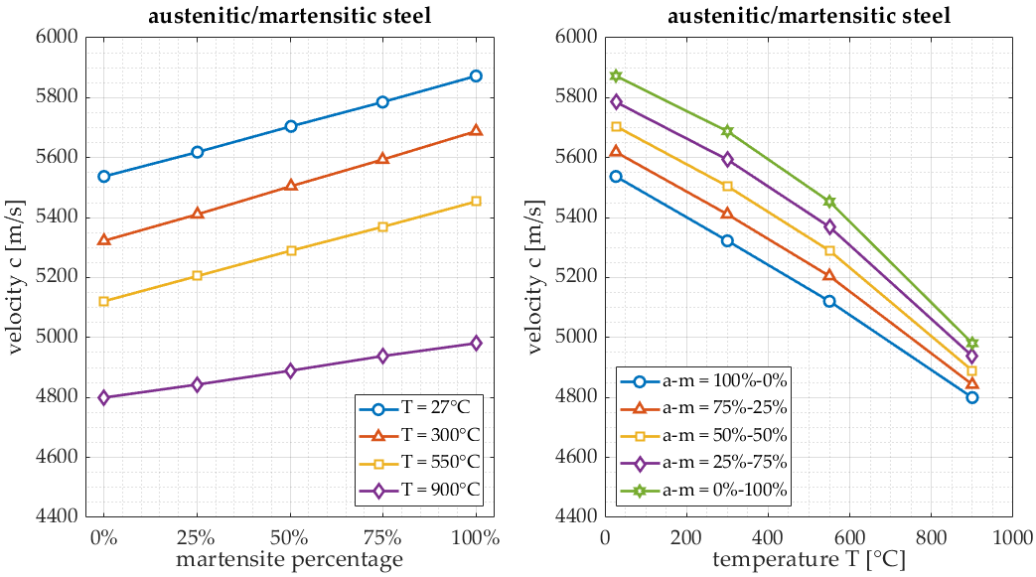

(**a**) (**b**)

Figure 17. (**a**) The wave velocity as function of the phase ratio, and (**b**) as function of temperature.

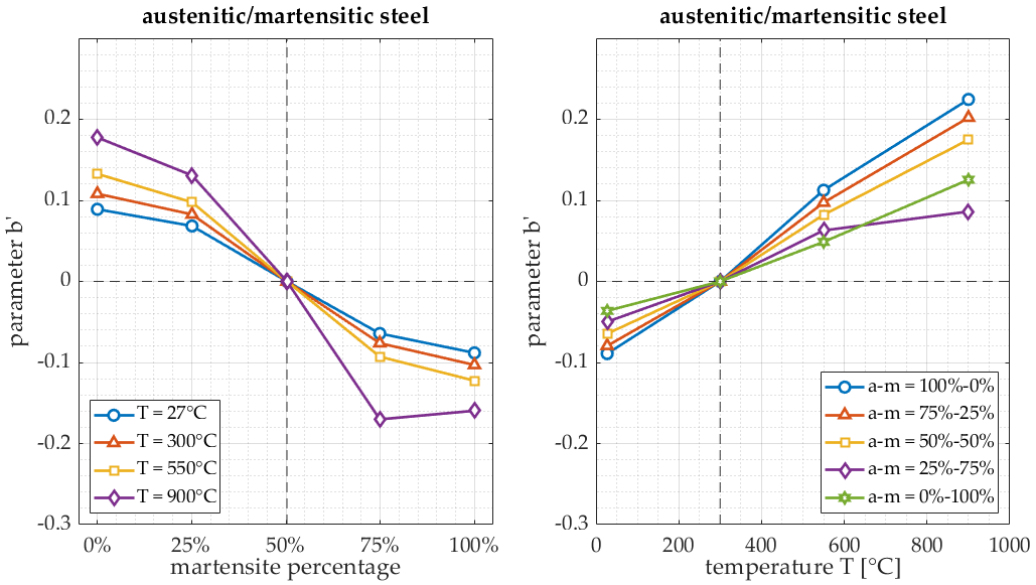

(**a**) (**b**)

Figure 18. (**a**) The relation between the phase ratio and parameter b' for austenite/martensite for the four temperatures; and (**b**) between temperature and parameter b'.

The curves appear to be depending on both phase ratio and temperature, as expected, although not in a linear fashion. A phase ratio change of 1% leads to an attenuation change of 0.002 (50% austenite at 300 °C, Figure 18a). A temperature change of 10 °C causes an attenuation change in the order of 0.003 (again 50% austenite at 300 °C, Figure 18b), which is of the same magnitude order. This shows that the effect of temperature is significant and cannot be ignored. Thus, assuming that the temperature can be measured on the order of 10 °C, the phase ratio can be estimated on the order of a percent.

It should be noted that in this series of simulations, both the average grain size and composition vary simultaneously in the samples. The average grain size varies from 15 µm at 100% austenite (0% martensite) down to 10 µm at 100% martensite. Since grain size also impacts the attenuation (as shown in the previous section), the results obtained are due to

the combined effect of grain size and composition, and not to composition only. This might have contributed to the non-linear shape of the observed curves.

Note that the accuracy with which phase ratios can be determined depends on the contrast between the phases (i.e., the differences in the corresponding elasticity matrices). Austenite and martensite differ much more than ferrite and martensite for instance, as can be seen in Figure 11. Hence it is expected that it will be even more difficult to determine phase ratios of a ferrite-martensite composite.

4. Summary and Discussion

Two main questions were posed in the introduction:

1. How accurate can grain size be determined from LUS simulations on various simulated microstructures and temperatures?
2. How accurate can the phase composition be determined from LUS simulations on various multiphase media and temperatures?

Both questions were dealt with, and the results are summarized here. Consequently, the question has been raised how well this can measured in practice, giving uncertainties in sample thickness and temperature fluctuations.

All simulations in Table 2 were performed at four different temperatures to see the impact of temperature on the results. As has been noticed in the previous section, temperature influences the elasticity matrix and density of a sample, and hence has an impact on the wave velocity and the amount of scattering (via grain contrast).

Two parameters were determined from the individual simulations: pressure wave velocity and frequency-dependent attenuation. Both are affected in a different way by the sample characteristics. An overview is given in Table 3, where the impact of grain size and phase fraction on the measurable velocity and on the attenuation is listed.

As mentioned, the temperature T and the sample thickness H should be known sufficiently accurately as well, since they have an impact on the wave velocity and attenuation as well. This leads to the list of cross-dependencies, as shown in Table 4. The values listed in the table lead to velocity or attenuation changes that are in the same order as caused by grain size variations of 1 µm or phase fraction variations of 10%, thus showing that no quantifiable dependency can be given for the sample thickness in case of the attenuation. Note that these dependencies scale linearly with the desired accuracy of the grain size and phase fractions.

Table 3. An overview of the influence of sample characteristics on measurable properties.

Sample Characteristic	Impact on the Pressure Wave Velocity	Impact on the Frequency Dependent Attenuation
Microstructure (grain size) *Reference points: Austenite: 15 µm Ferrite: 10 µm*	Austenite: velocity decrease of 1.6 m/s per µm. Ferrite: velocity decrease of 1.1 m/s per µm.	Austenite: attenuation increase of 0.03 per µm. Ferrite: attenuation increase of 0.011 per µm.
Phase volume fraction (austenite/martensite) *Reference point: fraction of 50%/50%*	Velocity increase of 37 m/s per 10 percent increase of the martensite fraction.	Attenuation increase of 0.02 per 10 percent increase of the martensite fraction.

Table 4. An overview of the cross-dependencies of temperature and thickness measurements.

Sample Characteristic	Measurement	Temperature Accuracy	Thickness Accuracy
Microstructure (grain size) *1 µm accuracy*	Velocity	Austenite: 2 °C Ferrite: 1 °C	Austenite: less than 10 µm Ferrite: less than 10 µm
	Attenuation	Austenite: 100 °C Ferrite: 100 °C	-
Phase volume fraction *10% accuracy*	Velocity	50 °C	In the order of 20 µm
	Attenuation	70 °C	-

4.1. Microstructure

Microstructures with various grain sizes were modelled. The finite-difference model was capable of dealing with RVEs with varying grain sizes and yields reliable results for grain sizes of 10 µm and larger. The frequency-dependent behavior of the attenuation as function of grain size agrees well with what was expected from grain scattering theory, as shown in Section 2.4. For smaller grain sizes differences are noticeable, which are expected to be due to a different scattering regime, or due to a too low grain-to-grid size ratio in the discretization.

From these simulations, it was observed that the wave velocities decrease with temperature, as was expected since the ratio of the elasticity coefficients and the density decreases. This is shown in Figures 12 and 13 where the velocity is plotted as function of temperature. For the two samples (pure austenite and pure ferrite), the temperature should be known accurately (order of 1 °C) and the velocity should be measured with high accuracy (order of 1 m/s) to capture grain size variations in the order of 1 µm. This is practically not considered feasible.

The attenuation coefficient $b'(d)$ is much less sensitive to temperature than the velocity, although temperature still plays a role in the attenuation. In Figures 14 and 15 the attenuation is shown for both pure austenite and pure ferrite with varying grain sizes. Estimation of grain size in the order of 1 µm based on the attenuation requires measurement of the attenuation in the order of 0.01 to 0.03 (ferrite and austenite, respectively), and measurement of the temperature in the order of ten degrees Celsius. This temperature measurement constraint is achievable. The impact of temperature was one order of magnitude smaller than in the velocity measurements.

4.2. Multiphase

Samples with varying ratios of austenite and martensite were modelled as well. Grain sizes are kept the same, and no texture has been applied.

In these multiphase simulations, the velocities as function of temperature are shown in Figure 17. As in the microstructure cases, both velocity and temperature measurements should be very accurate, when a small ratio difference is to be detected. A phase ratio change of 10% requires a velocity measurement accuracy in the order of a few tens of meters per second and a temperature accuracy in the order of a few tens of degrees Celsius. This is again challenging, as in the grain size case. Note that the multiphase simulation contains two phases with a relatively high contrast (i.e., difference in elastic properties): austenite and martensite. The less contrast there is between phases (as e.g., ferrite and martensite) the more difficult it will be to quantify the phase ratios.

Figure 18 shows the attenuation as function of phase ratio and temperature for an austenite-martensite mixture. If the phase ratio must be estimated with an accuracy of 10%, the corresponding attenuation change must be accurate in the order of 0.02. This order of change in attenuation can also be caused by a temperature fluctuation in the order of 70 °C. This indicates that estimation of the phase ratio using attenuation is moderately sensitive

to temperature fluctuations. In practice, determination of the phase in the order of 10% would be feasible in terms of temperature sensitivity.

5. Conclusions and Way Ahead

5.1. Conclusions

In order to estimate grain size variations in the order of 1 μm, the wave velocity must be known in the order of a few meters per seconds. In a similar fashion, an estimation of phase ratio variations in the order of 10%, requires a wave velocity accuracy of a few tens of meters per second. These accuracies are not feasible for practical use, since they lead to constraints towards temperature accuracy in the order of a few tens of degrees Celsius or less, and a sample thickness accuracy of less than 10 μm.

The attenuation coefficient is much less sensitive to temperature and sample thickness than the velocity and is considered a more promising alternative. The accuracy of 1 μm in grain size or 10% in phase composition can be obtained by measuring the attenuation with an accuracy in the order of a few hundredths. This leads to constraints to the temperature accuracy in the order of 70 °C.

5.2. Way Ahead

From these results, it can be concluded that the velocity on its own is insufficient to reliably quantify the grain size or the phase fraction, especially given the impact of small temperature or sample thickness variations. The attenuation is a more promising metric for quantification of grain size and/or phase fraction. Note that in case of phase fraction, the impact of grain size variation has not been taken into account, but that plays an important role as well in actual measurements. In the simulations the impact of grain size and phase fraction have been studied individually. Further research might focus on the use of a combination of velocity and attenuation, in order to be able to determine grain size and phase fraction within a sample at the same time.

In the previous analysis, the velocity was determined based on an observed time delay and the measured sample thickness. Especially this latter parameter requires a very accurate measurement, often in the order of micrometers. Since this is challenging, especially with local thickness variations, an alternative approach might be considered, such as the ratio of the pressure and shear wave velocities. The theoretical values of these velocities, derived from the elasticity matrices and densities, are shown in Figure 19a,b, and their ratios are shown in Figure 19c, again for the five samples and four temperatures. The advantage of this velocity ratio is that the thickness (and its inherent measurement error) drops out the equations, and hence the method does not require highly accurate thickness measurements.

Future investigations will be directed towards a simultaneous estimation of grain size and phase fraction, and/or texture. The challenge in this is that the setup for estimation of grain size might differ from the setup for estimation of phase fraction or texture. The current simulations have been performed with a relatively large source (laser spot) diameter, which is dedicated to grain size measurements. This setup generates pure pressure waves and hardly any shear waves. However, for texture and phase fraction measurements, the source diameter can be reduced, leading to the generation of shear waves as well. Alternatively, with a completely different setup (e.g., using piezo transducers) it is feasible to measure both pressure and shear waves simultaneously.

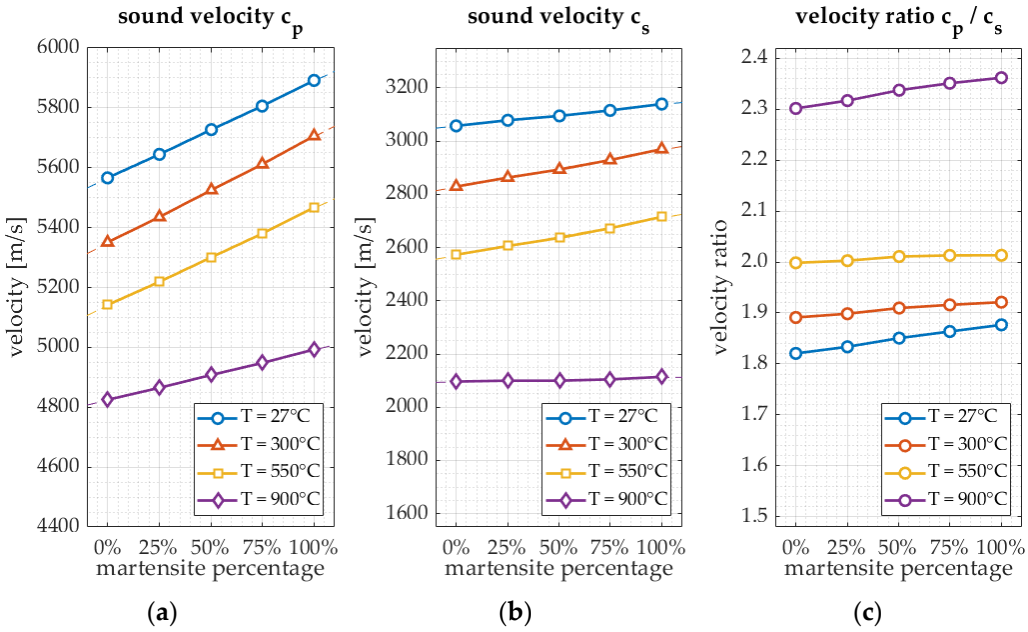

Figure 19. (**a**) The theoretical bulk pressure wave velocity c_p; (**b**) the theoretical bulk shear wave velocity c_s; and (**c**) their ratios c_p/c_s, as function of the martensite percentage for the martensite/austenite sample.

Author Contributions: Conceptualization, A.D., A.V. and F.V.d.B.; Data curation, F.V.d.B. and C.C.-C.; Formal analysis, A.D; Funding acquisition, F.V.d.B.; Investigation, A.D., A.V. and F.B; Methodology, A.D. and A.V.; Project administration, A.V. and F.V.d.B.; Resources, A.D., A.V., F.V.d.B. and C.C.-C.; Software, A.D. and A.V.; Supervision, A.V. and F.V.d.B.; Validation, A.D. and A.V.; Visualization, A.D.; Writing—original draft, A.D.; Writing—review & editing, A.D., A.V., F.V.d.B. and C.C.-C. All authors have read and agreed to the published version of the manuscript.

Funding: This work has been financed by European Union's Research Fund for Coal and Steel (RFCS) research program under grant agreement no. RFCS-2018-847296.

Acknowledgments: GLUS® data (Section 2.3) has been provided by Mikael Malmström (data curation, investigation), Anton Jansson (investigation), and Johan Lönnqvist (investigation), all affiliated with Swerim AB, 164 40 Kista, Sweden.

Conflicts of Interest: The authors declare no conflict of interest.

References

1. Hutchins, D.A.; Dewhurst, R.J.; Palmer, S.B. Laser generation as a standard acoustic source in metals. *Appl. Phys. Lett.* **1981**, *38*, 677–679. [CrossRef]
2. Aindow, A.M.; Dewhurst, R.J.; Palmer, S.B.; Scruby, C.B. Laser-based non-destructive testing techniques for the ultrasonic characterization of subsurface flaws. *NDT Int.* **1984**, *17*, 329–335. [CrossRef]
3. Scruby, C.B.; Smith, R.L.; Moss, B.C. Microstructural monitoring by laser-ultrasonic attenuation and forward scattering. *NDT Int.* **1986**, *19*, 307–313. [CrossRef]
4. Lévesque, D.; Kruger, S.E.; Lamouche, G.; Kolarik, R.; Jeskey, G.; Choquet, M.; Monchalin, J.-P. Thickness and grain size monitoring in seamless tube-making process using laser ultrasonics. *NDT E Int.* **2006**, *39*, 622–626. [CrossRef]
5. Liang, S.; Lévesque, D.; Legrand, N.; Zurob, H.S. Use of in-situ laser-ultrasonics measurements to develop robust models combining deformation, recovery, recrystallization and grain growth. *Materialia* **2020**, *12*, 100812. [CrossRef]
6. Majhi, S.; Mukherjee, A.; George, N.V.; Karaganov, V.; Uy, B. Corrosion monitoring in steel bars using Laser ultrasonic guided waves and advanced signal processing. *Mech. Syst. Signal Process.* **2021**, *149*, 107176. [CrossRef]
7. Ji, B.; Zhang, Q.; Cao, J.; Li, H.; Zhang, B. Non-contact detection of delamination in stainless steel/carbon steel composites with laser ultrasonic. *Optik* **2021**, *226*, 165893. [CrossRef]
8. Sarkar, S.; Moreau, A.; Militzer, M.; Poole, W.J. Evolution of Austenite Recrystallization and Grain Growth Using Laser Ultrasonics. *Metall. Mater. Trans. A* **2008**, *39*, 897–907. [CrossRef]
9. Garcin, T.; Schmitt, J.-H.; Militzer, M. In-situ laser ultrasonic grain size measurement in superalloy INCONEL 718. *J. Alloy. Compd.* **2016**, *670*, 329–336. [CrossRef]

10. Scherleitner, E.; Kerschbaummayr, C.; Haderer, W.; Reitinger, B.; Mitter, T.; Gruensteidl, C. Characterization of Microstructure Variations by Laser-Ultrasound during and after the Heat Treatment of Metals. *IOP Conf. Ser. Mater. Sci. Eng.* **2021**, *1178*, 012050. [CrossRef]
11. Malmström, M.; Jansson, A.; Hutchinson, B. Application of Laser-Ultrasonics for Evaluating Textures and Anisotropy. *Appl. Sci.* **2022**, *12*, 10547. [CrossRef]
12. Scruby, C.B.; Drain, L.E. *Laser Ultrasonics, Techniques and Applications*; Adam Hilger: Bristol, UK, 1990; ISBN 0-7503-0050-7.
13. Falkenström, M.; Engman, M.; Lindh-Ulmgren, E.; Hutchinson, B. Laser Ultrasonics for Process Control in the Metal Industry. *Nondestruct. Test. Eval.* **2011**, *26*, 237–252. [CrossRef]
14. Gusev, V.E.; Shen, Z.; Murray, T.W. Special Issue on Laser Ultrasonics. *Appl. Sci.* **2019**, *9*, 5561. [CrossRef]
15. Van den Berg, F. *Product Uniformity Control (PUC): Final Report*; Publications Office of the European Union: Luxembourg, 2020; ISBN 978-92-76-17320-5.
16. Monchalin, J.P. Laser-Ultrasonics: Principles And Industrial Applications. *E J. Nondestruct. Test.* **2020**, *1435*, 4934.
17. Everton, S.; Dickens, P.; Tuck, C.; Dutton, B. Using Laser Ultrasound to Detect Subsurface Defects in Metal Laser Powder Bed Fusion Components. *J. Miner. Met. Mater. Soc.* **2018**, *70*, 378–383. [CrossRef]
18. Bakre, C.; Afzalimir, S.H.; Jamieson, C.; Nassar, A.; Reutzel, E.W.; Lissenden, C.J. Laser Generated Broadband Rayleigh Waveform Evolution for Metal Additive Manufacturing Process Monitoring. *Appl. Sci.* **2022**, *12*, 12208. [CrossRef]
19. Dong, F.; Wang, X.; Yang, Q.; Yin, A.; Xu, X. Directional dependence of aluminum grain size measurement by laser-ultrasonic technique. *Mater. Charact.* **2017**, *129*, 114–120. [CrossRef]
20. Malmström, M.; Jansson, A.; Hutchinson, B.; Lönnqvist, J.; Gillgren, L.; Bäcke, L.; Sollander, H.; Bärwald, M.; Hochhard, S.; Lundin, P. Laser-Ultrasound-Based Grain Size Gauge for the Hot Strip Mill. *Appl. Sci.* **2022**, *12*, 10048. [CrossRef]
21. Keyvani, M.; Garcin, T.; Fabrègue, D.; Militzer, M.; Yamanaka, K.; Chiba, A. Continuous Measurements of Recrystallization and Grain Growth in Cobalt Super Alloys. *Metall. Mater. Trans. A* **2017**, *48*, 2363–2374. [CrossRef]
22. Feaugas, X.; Haddou, H. Grain-size effects on tensile behavior of nickel and AISI 316L stainless steel. *Metall. Mater. Trans. A* **2003**, *34*, 2329–2340. [CrossRef]
23. Watzl, G.; Grünsteidl, C.; Arnoldt, A.; Nietsch, J.A.; Österreicher, J.A. In situ laser-ultrasonic monitoring of elastic parameters during natural aging in an Al-Zn-Mg-Cu alloy (AA7075) sheet. *Materialia* **2022**, *26*, 101600. [CrossRef]
24. Wan, T.; Naoe, T.; Wakui, T.; Futakawa, M.; Obayashi, H.; Toshinobu, S. Effects of Grain Size on Ultrasonic Attenuation in Type 316L Stainless Steel. *Materials* **2017**, *10*, 753. [CrossRef]
25. Qin, W.; Li, J.; Liu, Y.; Kang, J.; Zhu, L.; Shu, D.; Peng, P.; She, D.; Meng, D.; Li, Y. Effects of grain size on tensile property and fracture morphology of 316L stainless steel. *Mater. Lett.* **2019**, *254*, 116–119. [CrossRef]
26. Abbasi Aghuy, A.; Zakeri, M.; Moayed, M.H.; Mazinani, M. Effect of grain size on pitting corrosion of 304L austenitic stainless steel. *Corros. Sci.* **2015**, *94*, 368–376. [CrossRef]
27. Su, Y.; Song, R.; Wang, T.; Cai, H.; Wen, J.; Guo, K. Grain size refinement and effect on the tensile properties of a novel low-cost stainless steel. *Mater. Lett.* **2020**, *260*, 126919. [CrossRef]
28. Tasan, C.C.; Hoefnagels, J.; Diehl, M.; Yan, D.; Roters, F.; Raabe, D. Strain localization and damage in dual phase steels investigated by coupled in-situ deformation experiments and crystal plasticity simulations. *Int. J. Plast.* **2014**, *63*, 198–210. [CrossRef]
29. Kadkhodapour, J.; Schmauder, S.; Raabe, D.; Ziaei-Rad, S.; Weber, U.; Bechtold, M. Experimental and numerical study on geometrically necessary dislocations and non-homogeneous mechanical properties of the ferrite phase in dual phase steels. *Acta Mater.* **2011**, *59*, 4387–4394. [CrossRef]
30. Ghassemi-Armaki, H.; Maaß, R.; Bhat, S.P.; Sriram, S.; Greer, J.R.; Kumar, K.S. Deformation response of ferrite and martensite in a dual-phase steel. *Acta Mater.* **2014**, *62*, 197–211. [CrossRef]
31. Pierman, A.-P.; Bouaziz, O.; Pardoen, T.; Jacques, P.J.; Brassart, L. The influence of microstructure and composition on the plastic behaviour of dual-phase steels. *Acta Mater.* **2014**, *73*, 298–311. [CrossRef]
32. Tasan, C.C.; Diehl, M.; Yan, D.; Bechtold, M.; Roters, F.; Schemmann, L.; Zheng, C.; Peranio, N.; Ponge, D.; Koyama, M.; et al. An Overview of Dual-Phase Steels: Advances in Microstructure-Oriented Processing and Micromechanically Guided Design. *Annu. Rev. Mater. Res.* **2015**, *45*, 391–431. [CrossRef]
33. Shivaprasad, S.; Pandala, A.; Krishnamurthy, C.V.; Balasubramaniam, K. Wave localized finite-difference-time-domain modelling of scattering of elastic waves within a polycrystalline material. *J. Acoust. Soc. Am.* **2018**, *144*, 3313–3326. [CrossRef]
34. Shivaprasad, S.; Krishnamurthy, C.V.; Pandala, A.; Saini, A.; Ramachandran, A.; Balasubramaniam, K. Numerical modelling methods for ultrasonic wave propagation through polycrystalline materials. *Trans. Indian Inst. Met.* **2019**, *72*, 2923–2932. [CrossRef]
35. Van Pamel, A.; Brett, C.R.; Huthwaite, P.; Lowe, M.J.S. Finite element modelling of elastic wave scattering within a polycrystalline material in two and three dimensions. *J. Acoust. Soc. Am.* **2015**, *138*, 2326–2336. [CrossRef]
36. Van Pamel, A.; Sha, G.; Rokhlin, S.I.; Lowe, M.J.S. Finite-element modelling of elastic wave propagation and scattering within heterogeneous media. *Proc. R. Soc. A* **2017**, *473*, 20160738. [CrossRef]
37. Hou, R.; Xu, B.; Xia, Z.; Zhang, Y.; Liu, W.; Glorieux, C.; Marsh, J.; Hou, L.; Liu, X.; Xiong, J. Numerical Simulation of Enhanced Photoacoustic Generation and Wavefront Shaping by a Distributed Laser Array. *Appl. Sci.* **2021**, *11*, 9497. [CrossRef]
38. Virieux, J. P-SV wave propagation in heterogeneous media: Velocity-stress finite-difference method. *Geophysics* **1985**, *51*, 889–901. [CrossRef]

39. Saenger, E.H.; Bohlen, T. Finite-difference modeling of viscoelastic and anisotropic wave propagation using the rotated staggered grid. *Geophysics* **2004**, *69*, 583–591. [CrossRef]
40. Celada-Casero, C.; Vercruysse, F.; Linke, B.; Smith, A.; Kok, P.; Sietsma, J.; Santofimia, M.J. Analysis of work hardening mechanisms in Quenching and Partitioning steels combining experiments with a 3D micro-mechanical model. *Mater. Sci. Eng. A* **2022**, *846*, 143301. [CrossRef]
41. Ghosh, G.; Olson, G.B. The isotropic shear modulus of multicomponent Fe-base solid solutions. *Acta Mater.* **2002**, *50*, 2655–2675. [CrossRef]
42. Rayne, J.A.; Chandrasekhar, B.S. Elastic Constants of Iron from 4.2 to 300 °K. *Phys. Rev.* **1961**, *122*, 1714–1716. [CrossRef]
43. Kim, S.A.; Johnson, W.L. Elastic constants and internal friction of martensitic steel, ferritic-pearlitic steel, and α-iron. *Mater. Sci. Eng. A* **2007**, *452–453*, 633–639. [CrossRef]
44. Gunkelmann, N.; Ledbetter, H.; Urbassek, H.M. Experimental and atomistic study of the elastic properties of α' Fe–C martensite. *Acta Mater.* **2012**, *60*, 4901–4907. [CrossRef]
45. Kamaya, M. A procedure for estimating Young's modulus of textured polycrystalline materials. *Int. J. Solids Struct.* **2009**, *46*, 2642–2649. [CrossRef]
46. Ledbetter, H.M. *Predicted Single-Crystal Elastic Constants of Stainless-Steel 316*; Report NBSIR-82-1667; National Bureau of Standards: Washington, DC, USA, 1982.
47. Gasteau, D.; Chigarev, N.; Ducousso-Ganjehi, L.; Gusev, V.; Jenson, F.; Calmon, P.; Tournat, V. Elastic constants of polycrystalline steel evaluated with laser generated surface acoustic waves. *J. Appl. Phys.* **2016**, *119*, 043103. [CrossRef]
48. Lethbridge, Z.A.D.; Walton, R.I.; Marmier, A.S.H.; Smith, C.W.; Evans, K.E. Elastic anisotropy and extreme Poisson's ratios in single crystals. *Acta Mater.* **2010**, *58*, 6444–6451. [CrossRef]
49. Hutchinson, B.; Malmström, M.; Lönnqvist, J.; Bate, P.; Ehteshami, H.; Korzhavyi, P.A. Elasticity and Wave Velocity in Fcc Iron (Austenite) at Elevated Temperatures–Experimental Verification of Ab-Initio Calculations. *Ultrasonics* **2018**, *87*, 44–47. [CrossRef]
50. Duijster, A.; Volker, A.; van den Berg, F.; Celada-Casero, C.; Melzer, S. Estimation of the stiffness tensor from Lamb wave velocity profiles measured on steel with different texture. *European Conference on Non-Destructive Testing 2023 (ECNDT 2023)*, 2023; in press.
51. Cho, Y.-G.; Kim, J.-Y.; Cho, H.-H.; Cha, P.-R.; Suh, D.-W.; Lee, J.K.; Han, H.N. Analysis of Transformation Plasticity in Steel Using a Finite Element Method Coupled with a Phase Field Model. *PLoS ONE* **2012**, *7*, e35987. [CrossRef] [PubMed]
52. Lyassami, M.; Shahriari, D.; Ben Fredj, E.; Morin, J.-B.; Jahazi, M. Numerical Simulation of Water Quenching of Large Size Steel Forgings: Effects of Macrosegregation and Grain Size on Phase Distribution. *J. Manuf. Mater. Process.* **2018**, *2*, 34. [CrossRef]
53. Dubois, M.; Militzer, M.; Moreau, A.; Bussière, J.F. A New Technique for the Quantitative Real-Time Monitoring of Austenite Grain Growth in Steel. *Scr. Mater.* **2000**, *42*, 867–874. [CrossRef]
54. Moreau, A.; Lévesque, D.; Sarkar, S. *Laser-Ultrasonics for Metallurgy: Overview and Latest Developments at NRC*; NRC Publications Archive; National Research Council: Ottawa, ON, Canada, 2013.
55. Kube, C.M.; Turner, J.A. Voigt, Reuss, Hill, and self-consistent techniques for modeling ultrasonic scattering. *AIP Conf. Proc.* **2015**, *1650*, 926–934.